[12]The intensity ratio of the R line to its sideband is about 1 : 2.5 at 77 °K. Neglecting nonradiative processes the total decay rate from the ^2E level is then 3.5 times as strong as the R-line radiative process. We also estimate in a similar manner that the total decay rate from the ^2E level of the tetragonal site is 2.4 times as strong as the N-line (6992 and 7038 Å) radiative process. From the measured 5 : 2 ratio between the transition strengths of the N and R lines we expect that the ratio of the decay rates from the ^2E levels of the cubic and tetragonal sites is $\frac{2}{5}\times 3.5/2.4 \approx \frac{3}{5}$, and the expected ratio of decay times is therefore 5 : 3.

[13]J. H. Parker, R. W. Weinert, and J. C. Castle, in *Optical Properties of Ions in Crystals*, edited by H. M. Crosswhite and H. W. Moos (Wiley, New York, 1967), p. 251.

[14]There is a ground-state splitting of 0.8 cm^{-1} in the rhombic site as measured by ESR. This would cause a broadening of the optical line on this site.

PHYSICAL REVIEW B VOLUME 7, NUMBER 1 1 JANUARY 1973

Tetragonal-Field Splittings of Levels in MgO : Cr^{3+} †

W. M. Fairbank, Jr.* and G. K. Klauminzer‡
Department of Physics, Stanford University, Stanford, California 94305
(Received 10 July 1972)

Detailed ground-state and selective-excitation traces reveal new $^2T_1$ and $^2T_2$ levels in MgO : Cr^{3+}. Computer diagonalizations are carried out to confirm the identity of the absorbing system. Detailed perturbation-loop calculations, which agree with results of the diagonalization, help to determine the causes of level splittings. Improved tetragonal-field parameters are given. The $^2T_2$ levels are assigned to the vacancy or pair-vacancy systems, whereas the $^2T_1$ levels are assigned to the cubic system. Assignment of other features to the $^2T_1$ levels of the vacancy system is tentative.

I. INTRODUCTION

When trivalent Cr^{3+} is substituted for divalent Mg^{2+} in a cubic MgO crystal, two Cr^{3+} ions and one vacant site replace three Mg^{2+} ions. Many Cr^{3+} ions enter purely cubic sites where there is no local charge compensation. Others (at most, 50%) enter sites with a vacancy in the [001] direction (tetragonal) and to a much lesser degree the [011] direction (rhombic).[1] In more strongly doped samples a "pair-vacancy" system of two Cr^{3+} ions adjacent to a vacancy is observed.

In absorption and fluorescence measurements the effects of the different systems sometimes overlap. However, by varying stress and concentration, the R line and sideband fluorescence of the cubic, tetragonal vacancy, and tetragonal pair-vacancy systems, have been separated.[2-5] Macfarlane analyzed the observed splittings of the $(t_2^3)\,^2E$ and $^4A_2$ levels in the vacancy system by perturbation-loop calculations for a weak tetragonal field.[6] Recent excited-state-absorption measurements have found two new sharp-line levels, $^2T_2(t_2^3)$ and $^2A_2(t_2^2 e)$, which required identification of the absorbing system.[7] Two new sharp lines in the expected region of the B lines ($^4A_2 \rightarrow {}^2T_2$) were found in the course of careful ground-state measurements needed to correct the excited-state-absorption data.[7] Intensity calculations were consistent with assigning all these new sharp-line transitions to the vacancy and pair-vacancy systems of tetragonal symmetry.

This paper, therefore, presents further analysis and system identification of the sharp-line transitions in MgO : Cr^{3+}. Detailed measurements of ground-state absorption determine the splitting of the $^2T_2$ level and the antiresonance parameters of interaction with the $^4T_1$ band. A new pair of $^2T_1$ levels seen photographically by Imbusch but not identified by him[4] is resolved in detail. The systems responsible for these lines are then identified by selective-excitation measurements which separate the ground-state-absorption contributions of the various systems. From the new experimental data better tetragonal-field parameters are found for the vacancy and pair-vacancy systems. Extended perturbation-loop calculations and diagonalization of the energy matrices with these parameters give a good fit to all observed levels.

II. EXPERIMENTAL

Ground-state-absorption measurements were made at low temperatures on three MgO : Cr^{3+} crystals of different concentrations varying from light yellow to dark green.[8] Samples No. 1 and 3 were mounted in the sample chamber of a Cary 14 spectrometer in the same double-walled glass Dewar used in excited-state-absorption measurements.[7] Cold nitrogen gas flowed through the Dewar to cool the crystals to approximately 100 °K. The rest of the sample chamber and the interior of the Cary were filled with warm dry nitrogen gas to prevent frosting. The lightly doped sample No. 2

was measured at 77 °K in order to obtain better resolution on the weak lines. This crystal was mounted in a vacuum in a copper block on the bottom of a cold finger filled with liquid nitrogen. The Dewar was placed in the sample chamber of the Cary so that light passed through the crystal and the quartz vacuum windows. Measurements on all three crystals were made from 2000 to 8000 Å using the 0–1 and 1–2 density slidewire, and then fine measurements were made using the 0–0.1 and 0.1–0.2 slidewire.

The observed ground-state spectrum for sample No. 1 is shown in Fig. 1. The usual $^4T_2$ and $^4T_1$ bands of Cr^{3+} are observed and then the absorption increases rapidly at the crystal-band-absorption edge. There are two sharp lines clearly visible around 20 000 cm^{-1} in the expected region of the lowest $^2T_2$ level. A fine trace of this region on a wavelength scale is shown in Fig. 2. These lines exhibit the characteristic antiresonance line shape due to interference between sharp lines and overlapping continuum described by Sturge, Guggenheim, and Pryce.[9] The theoretical line is a best fit to their formula:

$$\alpha(\omega) = \alpha_\beta(\omega) + \alpha_0'(q^2 + 2\xi q - 1)/(1+\xi^2)(1+q^2)\,,$$

where $\xi = (\omega - \omega_r)/\gamma$ and $\alpha_0' = \alpha_0(1+q^2)$. $\hbar\omega_r$ is the energy of the sharp state modified by interaction with the continuum, γ^{-1} is the lifetime of the sharp state against decay of the continuum, and $q^2\gamma$ may be interpreted as a measure of the strength of transitions to the modified sharp state relative to the continuum. In this region the continuum absorption $\alpha_\beta(\omega)$ is nearly linear with change in ω and is assumed to be so. The best-fitted values of these parameters for the different samples and lines are shown in Table I.

Absorption from the ground state to the $^2T_1$ level cannot be seen in Fig. 1 taken on the 0–1 density scale. However, a fine trace (Fig. 3) with the 0.0–0.1 slidewire shows two features at 6654.5 and 6682 Å, in agreement with the photographic measurements of Imbusch.[4]

A search was also made on all three crystals for ground-state absorption into the sharp $(t_2^2 e)\,^2A_2$

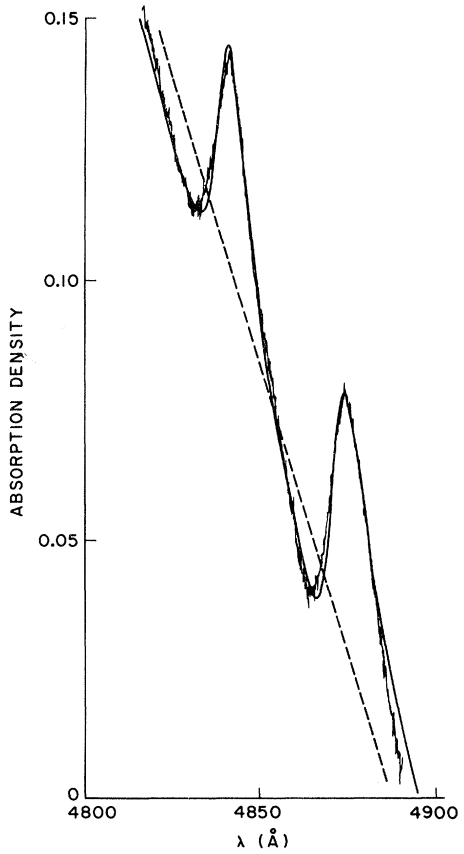

FIG. 2. Absorption spectrum of sample No. 1 in the region of the $^4A_2 \rightarrow {}^2T_2$ transition. The solid line is the theoretical antiresonance fit. The dashed line is the continuum absorption $\alpha_B(\omega)$.

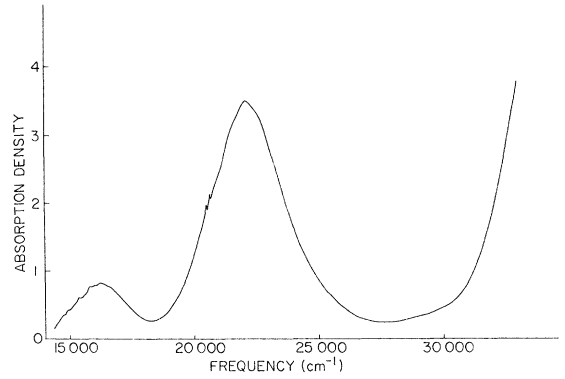

FIG. 1. Ground-state absorption spectrum for a medium concentration MgO : Cr^{3+} crystal (sample No. 1).

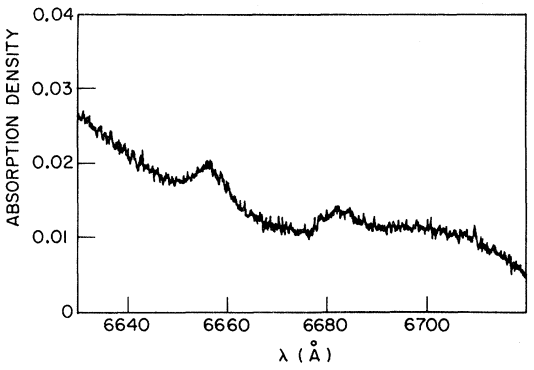

FIG. 3. Absorption spectrum of sample No. 1 in the region of the $^4A_2 \rightarrow {}^2T_1$ transition.

TABLE I. Best-fitted parameters for the $^2T_2$ levels in ground-state absorption.

MgO:Cr^{3+} crystal sample No.	Temp. (°K)	$\hbar\omega_r$ (cm^{-1})	$\hbar\gamma$ (cm^{-1})	α_0	q
1	104	20 522 ± 2	22	0.062	−1.5
		20 655 ± 2	20	0.056	−3.0
2	77	20 511 ± 4	18	0.011	−2.0
		20 650 ± 2	16	0.0085	−2.8
3	110	20 522 ± 5	25	0.036	−1.7
		20 662 ± 5	30	0.040	−2.9

level seen in excited-state absorption at 40 359 (vacancy) and 40 397 cm^{-1} (pair vacancy)[7] but was limited by the large slope of the band-edge absorption in this region. No evidence of sharp-line absorption into the $^2A_2$ level was seen.

The apparatus for the selective-excitation measurement is shown in Fig. 4. Light from a 600-W quartz halogen lamp passed through a water filter and was focused on the entrance slit of a Bausch and Lomb 0.5-m grating monochromator. Both slits were set at 2 mm, giving a resolution of 11 Å in the exciting radiation. The monochromator was driven continuously by a synchronous stepping motor. The wavelengths were calibrated by the lines of a Hg lamp and in the red by the position of direct scattering into the spectrometer set on the MgO R lines. Absolute wavelength accuracy was estimated to be ±20 Å, limited by inaccuracies in reading the monochromator scale. Relative wavelength errors in a given trace are smaller.

The monochromatic pumping light emerging from the exit slits was focused on the MgO crystal mounted in the cold-finger Dewar described above. A dark-green crystal (sample No. 4) was used so that fluorescence from all three systems (cubic, vacancy, and pair vacancy) would be present. Fluorescence from the front (toward the pump light) surface of the crystal was focused on the input slit of a Spex $\frac{3}{4}$-m spectrometer. The light was detected at the exit slit by an RCA C31000F photomultiplier tube cooled with dry ice. The signal was amplified by a Hewlett-Packard 425A microvoltmeter and recorded on a strip-chart recorder.

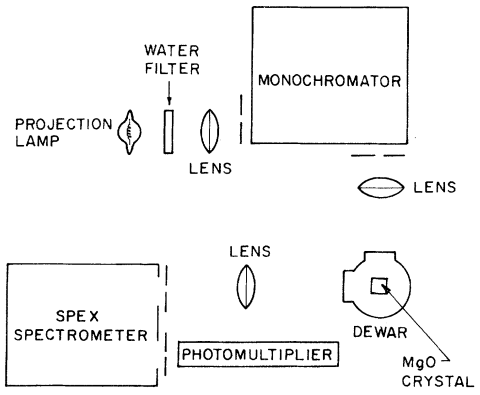

FIG. 4. Selective-excitation apparatus.

The spectrometer was first manually scanned over the region of the R-line fluorescence to check that the fluorescence lines could be resolved. It was then peaked on the 6981-, 7038-, and 7034-Å lines which originate from the cubic, vacancy, and pair-vacancy system, respectively, and selective-excitation traces were taken. To normalize the traces, the pump light from the monochromator to the crystal was measured. The Dewar was removed and a United Detector Technology PIN-10 photodiode was placed at the crystal position. The stepping motor swept the monochromator over the same region, and a strip-chart recording was taken in the same manner as above.

The recorded curves were digitized and then wavelength corrected on a computer. The pumping-light curve was corrected for photodiode efficiency by dividing by the digitized values from the manufacturer's efficiency curve. The selective-excitation curves were normalized by dividing by this calibrated pump-light curve and are shown in Fig. 5. The different peaks in these curves are identified and listed in Table II. The estimated error bars shown in Fig. 5 are large for higher energies because the pump-light level falls off rapidly in the blue region of the spectrum.

There are several outstanding features of these traces compared to the ground-state-absorption traces in Figs. 1–3. First, the $(t_2^3)\,^2T_2$-absorption

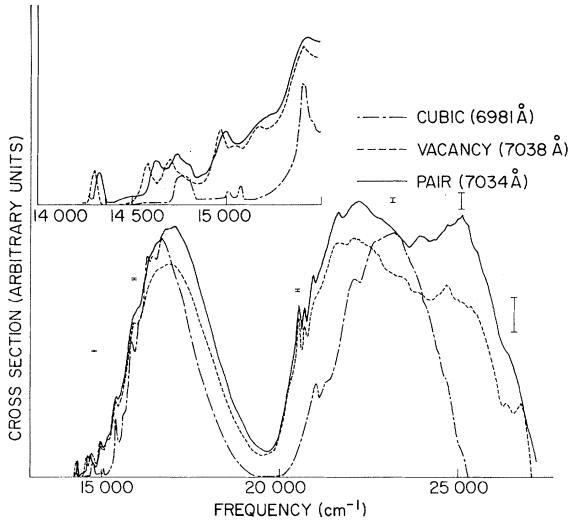

FIG. 5. Cross sections for selective excitation into the 6981-, 7038-, and 7034-Å R-line fluorescence of the cubic (dot-dashed curve), vacancy (dashed curve), and pair-vacancy (solid curve) systems, respectively. The insert shows an expanded view of the red region. Estimated error bars are shown.

TABLE II. Positions of the peaks in the selective-excitation traces.

	Cubic (6981 Å) (cm^{-1})	Vacancy (7038 Å) (cm^{-1})	Pair (7034 Å) (cm^{-1})
$a^2E(\pm 40)$	~14 300*	~14 200	~14 200*
	14 750 (sideband)	14 295	14 326
$a^2T_1(\pm 40)$	14 995	14 565	14 621
	15 060	14 692 (?)	14 735 (?)
		14 957	14 990
$a^2T_2(\pm 60)$	21 005	20 545	20 555
		20 695	20 706
$^4T_2(\pm 100)$	16 700	16 900	16 900
$a^4T_1(\pm 200)$	23 000	21 900	21 900
		24 900	24 900

lines appear only in the vacancy and pair-vacancy systems and at approximately the same positions. Second, the pair of $(t_2^3)\,^2T_1$ levels seen from the ground state appears only in the cubic trace. Another wide feature is seen near the R line in the cubic trace, but it has a similar shape and position relative to the R line as the R-line sidebands observed in fluorescence by Imbusch.[4] Assuming that the phonon density of states in the two t_2^3 states, $^4A_2$ and ^2E, is similar, the sidebands in absorption will be a mirror image of the emission sidebands on the opposite side of the R line. This feature is therefore assigned to be the R-line absorption sidebands. In the vacancy and pair traces, four peaks appear. The lowest-energy feature is the upper ^2E level. The other three are not inconsistent with assigning them to be sidebands of the ^2E level, but they could also be the $^2T_1$ levels of the tetragonally distorted systems. Third, the $^4T_1$ band is split in the vacancy and pair-vacancy systems, but the $^4T_2$ band is not greatly split; this splitting is hidden in the ground-state trace by the cubic-system absorption. Fourth, the pair-vacancy and vacancy-system energy levels almost coincide, indicating that the crystal fields for the two systems are nearly identical. Finally, the selective-excitation cross sections are nearly the same for the $^4T_2$ and $^4T_1$ bands for all three systems, but in ground-state absorption the $^4T_1$ band is much stronger. Thus the quantum efficiency of energy transfer from the $^4T_1$ band to the R line must be low at least for the cubic system. This explains why the fluorescence output of MgO:Cr^{3+} is low compared to ruby, even though the $^4T_1$-band-absorption cross sections are comparable. Assuming a higher quantum efficiency for the tetragonal systems than for the cubic system, one could also explain the enhanced fluorescence (a factor of 6 compared to absorption) of the tetragonal sites. Imbusch attributed this to energy transfer between systems.[4] But this would mean that $\frac{5}{6}$ of the tetragonal-system-fluorescence intensity comes from absorption in the bands of the cubic system, and all the traces in Fig. 5 should look like the cubic-system trace. In fact, the traces are quite different, indicating that intersystem energy transfer is responsible for not more than 10–20% of the noncubic fluorescence.

III. PERTURBATION LOOPS

The first extensive use of perturbation theory to evaluate energy-level splittings of cubic sites with a tetragonal-field perturbation was by Macfarlane.[6] He evaluated the splittings of the two states $^4A_2$ and a^2E (see Table VII for level designation), for which experimental data on the tetragonal-vacancy system in MgO:Cr^{3+} were available, in terms of the two tetragonal-field parameters δ and μ, for the vacancy system.[10] He found $\delta \approx 1800$ cm^{-1} and $\mu \approx -180$ cm^{-1}. However, these parameters are not valid because the wrong sign of the splitting of the ground state was used in the calculation.

The new experimental data in this paper provide the positions and splittings of the $^4T_2$, a^4T_1, a^2T_2, and possibly the a^2T_1 levels in the vacancy and pair-vacancy systems. It is therefore of interest to extend the perturbation calculations to include these states or to do a complete diagonalization in order to get a better fit for the parameters δ and μ. Inconsistent splittings can then indicate wrong system assignments of the observed transitions. Although a diagonalization was done and gives the more exact theoretical results, the perturbation calculations are presented in order to indicate the origin of the splittings and the accuracy of the perturbation expansion.

Time-independent perturbation theory gives the following formulas for the first- through fifth-order corrections to the energies E_n determined from a diagonalization of the zero-order Hamiltonian[11] $\mathcal{H}_0$:

$$E_n^{(1)} = U_{nn}\,, \tag{1}$$

$$E_n^{(2)} = \sum_{p\neq n} \frac{U_{np}\,U_{pn}}{E_n - E_p}\,, \tag{2}$$

$$E_n^{(3)} = \sum_{p,q\neq n} \frac{U_{np}\,U_{pq}\,U_{qn}}{(E_n-E_p)(E_n-E_q)} - \sum_{p\neq n} \frac{U_{np}\,U_{pn}\,U_{nn}}{(E_n-E_p)^2}\,, \tag{3}$$

$$E_n^{(4)} = \sum_{p,q,r\neq n} \frac{U_{np}\,U_{pq}\,U_{qr}\,U_{rn}}{(E_n-E_p)(E_n-E_q)(E_n-E_r)} - \sum_{p,q\neq n} \frac{U_{np}\,U_{pq}\,U_{qn}\,U_{nn}}{(E_n-E_p)(E_n-E_q)}\left(\frac{1}{E_n-E_p}+\frac{1}{E_n-E_q}\right) - \sum_{p,q\neq n} \frac{U_{np}\,U_{pn}\,U_{nq}\,U_{qn}}{(E_n-E_p)^2(E_n-E_q)} + \frac{1}{2}\sum_{p\neq n} \frac{U_{np}\,U_{pn}\,U_{nn}^2}{(E_n-E_p)^3}\,, \tag{4}$$

$$E_n^{(5)} = \sum_{p,q,r,s\neq n} \frac{U_{np}\,U_{pq}\,U_{qr}\,U_{rs}\,U_{sn}}{(E_n-E_p)(E_n-E_q)(E_n-E_r)(E_n-E_s)} - \cdots . \quad (5)$$

Here $U_{ij}=\langle i|\mathcal{H}_I|j\rangle$, where $\mathcal{H}_I$ is the Hamiltonian of the perturbation and $|i\rangle$ are the eigenstates of $\mathcal{H}_0$.

For atoms of configuration d^3 in a nearly cubic crystalline field with a small tetragonal field, the Hamiltonian is

$$\mathcal{H}=H_C(D_q)+H_E(B,C)+H_T(\delta,\mu)+H_{so}(\zeta,\zeta'), \quad (6)$$

where H_C, H_E, H_T, and H_{so} are, respectively, the cubic field, electrostatic Coulomb interaction, tetragonal field, and spin-orbit Hamiltonians. The zero-order Hamiltonian $\mathcal{H}_0$ is taken to be H_C plus the diagonal terms of H_E.[6] The rest are treated as $\mathcal{H}_I$. A strong-field cubic basis is chosen for the perturbation calculations so that H_C is a diagonal matrix.

One notices in Eqs. (1)–(5) that every state occurs twice, and hence can be represented as a line connecting two interactions, which are represented as dots. Using this representation convention, all the nonzero perturbation "loops" through third order involving the tetragonal field and the major fourth-order loops for the a^2T_2 and a^2T_1 states are shown in Fig. 6. All nonzero first- and second-order loops and significant higher-order loops for the $^4T_2$ and a^4T_2 states are also shown. The designations of the states are explained in Table VII.

TABLE III. Changes in sign of state from GII.

	Tanabe and Sugano	GI
$a\,^2E\ (t_2^3)$	+	+
$b\,^2E\ [t_2^2(^1E)e]$	−	+
$c\,^2E\ [t_2^2(^1A_1)e]$	+	+
$d\,^2E\ (e^3)$	+	+
$^4A_2\ (t_2^3)$	+	+
$^2A_1\ [t_2^2(^1E)e]$	−	+
$^2A_2\ [t_2^2(^1E)e]$	−	+
$^4T_2\ [t_2^2(^3T_1)e]$	−	−
$a\,^4T_1\ [t_2^2(^3T_1)e]$	+	−
$b\,^4T_1\ [t_2e^2(^3A_2)]$	−	+
$a\,^2T_1\ (t_2^3)$	+	+
$b\,^2T_1\ [t_2^2(^3T_1)e]$	+	−
$c\,^2T_1\ [t_2^2(^1T_2)e]$	−	+
$d\,^2T_1\ [t_2e^2(^3A_2)]$	−	+
$e\,^2T_1\ [t_2e^2(^1E)]$	+	+
$a\,^2T_2\ (t_2^3)$	+	+
$b\,^2T_2\ [t_2^2(^3T_1)e]$	−	−
$c\,^2T_2\ [t_2^2(^1T_2)e]$	+	−
$d\,^2T_2\ [t_2e^2(^3A_2)]$	+	+
$e\,^2T_2\ [t_2e^2(^1E)]$	−	−

TABLE IV. Tetragonal-field matrix elements (STK basis).

Γ_1	Γ_2	$\langle\Gamma_1\|V(E)\|\Gamma_2\rangle$	Γ_1	Γ_2	$\langle\Gamma_1\|V(E)\|\Gamma_2\rangle$
a^2T_1x	a^2T_2x	δ	c^2T_2x	c^2T_2x	$-\frac{1}{3}\delta+\frac{1}{4}\mu$
a^2T_1y	a^2T_2y	$-\delta$	c^2T_1y	c^2T_1y	$-\frac{1}{3}\delta-\frac{1}{4}\mu$
^4T_2x	^4T_2x	$-\frac{1}{3}\delta-\frac{1}{4}\mu$	c^2T_1y	c^2T_2y	$\frac{1}{4}\sqrt{3}\mu$
^4T_2y	^4T_2y	$-\frac{1}{3}\delta-\frac{1}{4}\mu$	c^2T_2y	c^2T_2y	$-\frac{1}{3}\delta+\frac{1}{4}\mu$
^4T_2z	^4T_2z	$\frac{2}{3}\delta+\frac{1}{2}\mu$	c^2T_1z	c^2T_1z	$\frac{2}{3}\delta+\frac{1}{2}\mu$
^4T_2x	a^4T_1x	$\frac{1}{4}\sqrt{3}\,\mu$	c^2T_2z	c^2T_2z	$\frac{2}{3}\delta-\frac{1}{2}\mu$
^4T_2y	a^4T_1y	$-\frac{1}{4}\sqrt{3}\,\mu$	b^4T_1x	b^4T_1x	$\frac{1}{3}\delta$
a^4T_1x	a^4T_1x	$-\frac{1}{3}\delta+\frac{1}{4}\mu$	b^4T_1y	b^4T_1y	$\frac{1}{3}\delta$
a^4T_1y	a^4T_1y	$-\frac{1}{3}\delta+\frac{1}{4}\mu$	b^4T_1z	b^4T_1z	$-\frac{2}{3}\delta$
a^4T_1z	a^4T_1y	$\frac{2}{3}\delta-\frac{1}{2}\mu$	d^2T_1x	d^2T_1x	$\frac{1}{3}\delta$
b^2Eu	c^2Eu	$\frac{2}{3}\delta$	d^2T_1y	d^2T_1y	$\frac{1}{3}\delta$
b^2Eu	$^2A_1$	$\frac{2}{3}\delta+\frac{1}{2}\mu$	d^2T_1z	d^2T_1z	$-\frac{2}{3}\delta$
b^2Ev	c^2Ev	$-\frac{2}{3}\delta$	e^2T_1x	e^2T_1x	$\frac{1}{3}\delta$
b^2Ev	$^2A_2$	$-\frac{2}{3}\delta+\frac{1}{2}\mu$	e^2T_1y	e^2T_1y	$\frac{1}{3}\delta$
c^2Eu	c^2Eu	$-\frac{1}{2}\mu$	e^2T_1z	e^2T_1z	$-\frac{2}{3}\delta$
c^2Eu	$^2A_1$	$-\frac{2}{3}\delta$	e^2T_2x	e^2T_2x	$\frac{1}{3}\delta$
c^2Ev	c^2Ev	$\frac{1}{2}\mu$	e^2T_2y	e^2T_2y	$\frac{1}{3}\delta$
c^2Ev	$^2A_2$	$\frac{2}{3}\delta$	e^2T_2z	e^2T_2z	$-\frac{2}{3}\delta$
b^2T_1x	b^2T_1x	$-\frac{1}{3}\delta+\frac{1}{4}\mu$	d^2Eu	d^2Eu	$\frac{1}{2}\mu$
b^2T_1x	b^2T_2x	$\frac{1}{4}\sqrt{3}\,\mu$	d^2Ev	d^2Ev	$-\frac{1}{2}\mu$
b^2T_2x	b^2T_2x	$-\frac{1}{3}\delta-\frac{1}{4}\mu$	d^2T_2x	d^2T_2x	$\frac{1}{3}\delta$
b^2T_1y	b^2T_1y	$-\frac{1}{3}\delta+\frac{1}{4}\mu$	d^2T_2x	e^2T_1x	$\frac{1}{2}\sqrt{3}\,\mu$
b^2T_1y	b^2T_2y	$-\frac{1}{4}\sqrt{3}\,\mu$	d^2T_2x	e^2T_2x	$-\frac{1}{2}\mu$
b^2T_2y	b^2T_2y	$-\frac{1}{3}\delta-\frac{1}{4}\mu$	d^2T_2y	d^2T_2y	$\frac{1}{3}\delta$
b^2T_1z	b^2T_1z	$\frac{2}{3}\delta-\frac{1}{2}\mu$	d^2T_2y	e^2T_1y	$-\frac{1}{2}\sqrt{3}\,\mu$
b^2T_2z	b^2T_2z	$\frac{2}{3}\delta+\frac{1}{2}\mu$	d^2T_2y	e^2T_2y	$-\frac{1}{2}\mu$
c^2T_1x	c^2T_1x	$-\frac{1}{3}\delta-\frac{1}{4}\mu$	d^2T_2z	d^2T_2z	$-\frac{2}{3}\delta$
c^2T_1x	c^2T_2x	$-\frac{1}{4}\sqrt{3}\,\mu$	d^2T_2z	e^2T_2z	$+\mu$

To convert from one author's basis to another author's basis. This can be calculated from the phase differences of the Clebsch–Gordan coefficients given in GII and the phase differences of the coefficients of fractional parentage. A comparison of the phases of the cubic basis states of GI, GII, and STK is given in Table III.

The easiest method of calculating the tetragonal-field matrix elements in the cubic basis is with the V and W coefficients of Griffith (GII).[12] The spin-orbit matrix elements, however, are most easily calculated with the tables of Sugano, Tanabe, and Kamimura (STK).[13–15] In addition, the cubic-field matrices are already calculated in the STK basis.[13] Care must be taken in using the tables of different authors, since their cubic basis states may differ in phase. One needs a table of relative phases of states to convert from one author's basis to another author's basis. This can be calculated from the phase differences of the Clebsch–Gordan coefficients given in GII and the phase differences of the coefficients of fractional parentage. A comparison of the phases of the cubic basis states of GI, GII, and STK is given in Table III.

The matrix elements of the tetragonal field in terms of δ and μ were calculated from GII tables on a computer. All nonzero matrix elements converted to the STK basis are given in Table IV. All spin-orbit matrix elements were also calculated on the computer, but are not given since there are several thousand nonzero elements. This large number is a result of the cubic basis being an inconvenient basis for the spin-orbit interaction. Because all diagonal spin-orbit matrix elements are zero

FIG. 6. (a) Perturbation loops for tetragonal-field splittings for the $^4A_2$, $a\ ^2E$, $^4T_2$, and $a\ ^4T_1$ states in a nearly cubic crystal. (b) Perturbation loops for tetragonal-field splittings for the $a\ ^2T_1$ and $a\ ^2T_2$ states in a nearly cubic crystal.

and many nondiagonal matrix elements exist, perturbation expansions for the spin-orbit interaction in this basis do not converge rapidly. Hence, pure spin-orbit loops are neglected; it follows that the ξ and η components of T_2 states and α and β components of T_1 states will remain degenerate. This is not an important defect for most states however, because the spin-orbit parameter is much smaller

TABLE V. Numerators for the individual perturbation loops. The denominators are given in Eqs. (1)–(5). The evaluated splitting contributions in cm^{-1} for the $MgO:Cr^{3+}$ vacancy site are given. The parameter values of Table VI are used.

$^4T_2$	$(\pm\frac{1}{2})-(\pm\frac{3}{2})$		a^2E	$u-v$	
(3a)	$-\frac{8}{9}\delta\zeta'^2-\frac{2}{3}\mu\zeta'^2$	0.199	(3a)	$96\delta B^2$	35.4
(3b)	$\frac{8}{9}\delta\zeta'^2+\frac{2}{3}\mu\zeta'^2$	−0.058	(3b)	$-72\mu B^2$	45.9
(4a)	$-\frac{2}{3}\delta^2\zeta'^2$	0.010	(3c)	$-\frac{8}{9}\delta\zeta'^2-\frac{2}{3}\mu\zeta'^2$	11.3
(4b)	$8B\delta\zeta'^2+6B\mu\zeta'^2$	0.013	(3d)	$\delta\zeta'^2+\frac{3}{4}\mu\delta'^2$	−0.22
			(3e)	$-\frac{1}{9}\delta\zeta'^2-\frac{1}{12}\mu\zeta'^2$	0.025
			(4a)	$\frac{1}{3}\delta^2\,\zeta^2$	−1.69
$^4T_2$	$\zeta-(\xi,\ \eta)$		$a\,^4T_1$	$\gamma-(\alpha,\ \beta)$	
(1a)	$\delta+\frac{3}{4}\mu$	−1050.0	(1a)	$\delta-\frac{3}{4}\mu$	3750.0
(2a)	$-\frac{3}{16}\mu^2$	345.9	(2a)	$-\frac{3}{16}\mu^2$	−345.9
(3a)	$\frac{1}{16}\delta\mu^2-\frac{3}{64}\mu^3$	77.9	(3a)	$-36\delta B^2$	−82.2
(3b)	$-\frac{1}{16}\delta\mu^2-\frac{3}{64}\mu^3$	21.8	(3b)	$\frac{1}{16}\delta\mu^2+\frac{3}{64}\mu^3$	−21.8
(4a)	$\frac{9}{256}\mu^4$	−21.6	(3c)	$-\frac{1}{16}\delta\mu^2+\frac{3}{64}\mu^3$	−77.9
(4b)	$-\frac{3}{32}\mu^2\,(\frac{1}{3}\delta+\frac{1}{4}\mu)^2$	0.7	(4a)	$\frac{9}{256}\mu^4$	21.6
(4c)	$(\frac{1}{8}\mu^2\delta-\frac{3}{32}\mu^3)\,(\frac{1}{3}\delta+\frac{1}{4}\mu)$	9.8	(4b)	$-\frac{3}{32}\mu^2(-\frac{1}{3}\delta+\frac{1}{4}\mu)^2$	−8.8
(5a)	$-\frac{9}{4}\mu^2\delta B^2$	−0.8	(4c)	$(\frac{1}{8}\mu^2\delta+\frac{3}{32}\mu^3)\,(\frac{1}{3}\delta-\frac{1}{4}\mu)$	−9.8
			(4d)	$24\delta^2B^2-18\delta\mu B^2$	−15.4
a^2T_1	$\gamma-(\alpha,\ \beta)$		a^2T_2	$\zeta-(\xi,\ \eta)$	
(2a)	$-\delta^2$	269.7	(2a)	$-\delta^2$	−269.7
(3a)	$9B^2\delta-\frac{27}{4}B^2\mu$	16.7	(3a)	$27B^2\delta+\frac{81}{4}B^2\mu$	−28.9
(3b)	$9B^2\delta+\frac{27}{4}B^2\mu$	−7.8	(3b)	$75B^2\delta-\frac{225}{4}B^2\mu$	234.9
(3c)	$-12B^2\delta$	−2.7	(3c)	$-\frac{1}{6}\delta\zeta'^2-\frac{1}{8}\mu\zeta'^2$	0.41
(3d)	$-\frac{1}{6}\ \delta\xi'^2-\frac{1}{8}\mu\xi^2$	3.2	(3d)	$-\frac{1}{2}\delta\xi'^2+\frac{3}{8}\mu\xi'^2$	−27.0[a]
(3e)	$-\frac{1}{2}\delta\zeta'^2+\frac{3}{8}\mu\zeta'^2$	−2.0	(3e)	$\frac{1}{2}\mu\zeta'^2$	−0.13
(3f)	$\delta\zeta'^2+\frac{3}{4}\mu\zeta'^2$	−0.24	(3f)	$-\frac{1}{16}\delta\zeta'^2+\frac{3}{64}\mu\zeta'^2$	−0.08
(3g)	$-\frac{1}{16}\delta\zeta'^2+\frac{3}{64}\mu\zeta'^2$	−0.03	(3g)	$-\frac{1}{16}\delta\zeta'^2-\frac{3}{64}\mu\zeta'^2$	0.04
(3h)	$-\frac{1}{16}\delta\zeta'^2-\frac{3}{64}\mu\zeta'^2$	−0.01	(3h)	$-\frac{1}{48}\delta\zeta'^2-\frac{1}{64}\mu\zeta'^2$	0.02
(3i)	$-\frac{1}{48}\delta\zeta'^2-\frac{1}{64}\mu\zeta'^2$	0.005	(3i)	$-\frac{3}{16}\delta\zeta'^2+\frac{9}{64}\delta\zeta'^2$	−0.14
(3j)	$-\frac{3}{16}\delta\zeta'^2+\frac{9}{64}\mu\zeta'^2$	−0.07	(3j)	$-\frac{9}{32}\mu\zeta'^2$	0.33
(3k)	$-\frac{3}{32}\mu\zeta'^2$	0.05	(3k)	$-\frac{3}{32}\mu\zeta'^2$	0.14
(3l)	$-\frac{9}{32}\mu\zeta'^2$	0.14	(3l)	$-\frac{1}{3}\delta\zeta'^2+\frac{1}{4}\mu\zeta'^2$	−0.36
(4a)	δ^4	−10.8	(3m)	$-\frac{2}{3}\delta\zeta'^2$	−0.11
			(3n)	$-\delta\,(4B+2C)^2$	−51.0
			(3o)	$-4\delta B^2$	−0.12
			(3p)	$(24B^2+12BC)\mu$	−17.5
			(4a)	δ^4	10.8

[a]Observed energy levels used for denominators.

than the tetragonal-field parameter yielding small spin-orbit splittings compared to tetragonal-field splittings, as is seen in the complete diagonalization.

IV. ANALYSIS

The evaluation of the perturbation loops in Fig. 6 is given in Table V. To save space, only the numerators are shown. The energy denominators for each term can be determined from Eqs. (1)–(5). All factors of 2 arising from these equations are included in the numerators.

The most direct method of determining the tetragonal-field parameters is from the splitting of the $^4T_2$ and $a\,^4T_1$ states, the only experimentally observed levels which are split in first order. One must be cautious, however, in interpreting band splittings, since the Jahn–Teller distortions of these states can quench or enhance small crystal field splittings and can even disguise the splittings with a Jahn–Teller splitting. Quenching is common when the splitting operator, such as a trigonal field or a spin-orbit interaction, is nondiagonal in the basis of the tetragonal ϵ distortion, the predominant distortion in bands of $3d$ ions in octahedral coordination.[16] A tetragonal-crystal-field perturbation, on the other hand, is diagonal in this basis, and should not be greatly quenched or enhanced. A Jahn–Teller splitting is unlikely in the case of transitions to T states because coupling to ϵ distortion can only cause splitting when the spin-orbit coupling is much larger than the vibrational frequency.[16] This is not the case for $3d$ ions, as the lack of Jahn–Teller splitting in the cubic system bands in Fig. 5 indicates.

Thus, for $3d$ ions one expects the observed splitting of the bands to be a valid means of determining the tetragonal-field parameters. In Fig. 5 the $^4T_1$ splitting is 3000 cm^{-1}, and the $^4T_2$ splitting is too small to be resolved. However, the $^4T_2$ bands of the tetragonal systems are approximately 600 cm^{-1} wider than in the cubic system. This may be due to an underlying splitting of 600 cm^{-1} in the tetragonal system.

Since polarization measurements were not made, the sign of these splittings is not known. Thus these two splittings do not determine the two parameters δ and μ. Point-charge measurements for compressive stress on MgO:Cr^{3+} predict that δ is positive and μ negative.[2,6] Opposite signs are expected for extensive stress. Since the vacancy R lines lie to the red of the cubic R lines and compressive stresses produce red shifts, Schawlow concludes that the vacancy produces a net compression of the octahedron.[17] Thus $\delta > 0$ and $\mu < 0$ are expected. Indeed, one sees in Table V that this choice of signs is necessary to fit the observation[17] that the ^2E v state lies lower than the u state in the vacancy system.

Since the $^4A_2$ splitting derives largely from the $^4T_2$ splitting, the sign of the $^4A_2$ splitting establishes the sign of the $^4T_2$ splitting. The parameters are now completely determined. The experimentally observed coincidence of the ξ and η states of the $a\,^2T_2$ level affords a fine determination of δ. This gives $\delta = 1350 \pm 50$ cm^{-1} practically independent of the value of μ. A best fit to all splitting gives $\mu = -3200 \pm 300$ cm^{-1}. This gives $\delta = -2.4\,\mu$, which is very close to the ratio for applied stress in MgO:Cr^{3+}, $\delta = -2.1\,\mu$.

With these parameter values the splitting contributions of all the perturbation loops are evaluated numerically in Table V to identify the important loops. In this evaluation, higher-order effects in the electrostatic repulsion parameters B and C are taken into account by using the eigenfunction-mixture coefficients and the energies for denominators from a diagonalization of the whole cubic Hamiltonian $H_0' = H_C + H_E$. These "quasi-nth-order" evaluations give a slightly more accurate numerical result by taking the complete electrostatic configuration interaction into account without significantly changing the meaning of the perturbation loops diagrammed in Fig. 6. The only problem arises in the $a\,^2T_2$ ($3d$) perturbation loop, where the calculated energy denominator is too small, giving an anomalously large splitting contribution of -331 cm^{-1}. Cubic-field calculations for the $3d^3$ system using $\alpha = 0$ always place the $^2T_2$ level hundreds of cm^{-1} too high, leaving it too close to the $a\,^4T_1$ level.[7] In addition, as the tetragonal field is turned on, the $a\,^4T_1$ γ state is displaced to higher energies. In this case it is necessary to use the experimental energy levels for calculating the energy denominators. The splitting contribution is now reduced to -27 cm^{-1}. The totals of all the splitting contributions for each state are listed in Table VI.

TABLE VI. A comparison of the tetragonal-field splittings in cm^{-1} calculated by perturbation loops by diagonalization with the experimental values for the MgO:Cr^{3+} vacancy system. The parameters used in the theoretical calculations were: $Dq = 1645$, $B = 530$, $C = 3410$, $\zeta = \zeta' = 240$, $\alpha = 0$, $\delta = 1350$, and $\mu = -3200$ cm^{-1}.

Perturbation loops		Diagonalization	Expt.
$^4A_2$ $(\frac{1}{2} - \frac{3}{2})$	0.164	0.146	0.16
a^2E $(u - v)$	90.7	87.4	94
$a\,^2T_1(\gamma - \alpha,\ \beta)$	266.2	209.2	265
		278.0	390
$a\,^2T_2$ $(\zeta - \xi,\ \eta)$	−148.2	−154.7	−133
		−161.2	
$^4T_2$ $(\zeta - \xi,\ \eta)$	−615	−665[a]	±600
$a\,^4T_1(\gamma - \alpha,\ \beta)$	3210	2973[a]	±3000

[a]Average over states split by the spin-orbit interaction.

TABLE VII. Results of diagonalization of the energy matrices compared with the observed energy levels for the $MgO:Cr^{3+}$ cubic and vacancy systems. All values are in cm^{-1}.

	Cubic			Vacancy		Pair
	Diagonalized	Observed		Diagonalized	Observed	Observed
$^4A_2(t_2^3)$	0	0	E'	0	0	
			E''	0.145	0.16	
$a^2E\ (t_2^3)$	14058	14319	E''	14212	14205	14213
			E'	14299	14298	14304
$a^2T_1(t_2^3)$	14654	14961	E'	14458	14565 } (?)	14621 } (?)
	14707	15019	E''	14535	14692 }	14735 }
			E'	14743	14957 }	14990 }
$^4T_2[t_2^2(^3T_1)e]$	15805	16300	E'	16446	16900	17000
	15868		E''	16449		
	15991		E'	17078		
	16008		E''	17106		
			E'	17108		
			E''	17142		
$a^2T_2(t_2^3)$	20703		E''	21169	20522	20522
	20798		E'	21350	20655	20655
			E''	21351		
$a^4T_1[t_2^2(^3T_1)e]$	22098	22100	E''	21898	22000	22000
	22131		E''	21982	24800	25000
	22132		E'	21984		
			E'	22030		
			E'	24960		
			E''	24971		
$^2A_1[t_2^2(^1E)e]$	27875		E'	29406		
$b^2T_2[t_2^2(^3T_1)e]$	30137		E'	30611		
	30187		E''	30745		
			E''	30991		
		29820				
$c^2T_1[t_2^2(^1T_2)e]$	30277		E'	31121		
	30439		E'	32372		
			E''	32442		
$b^2E[t_2^2(^1E)e]$	31790		E'	32749		
			E''	32858		
$b^2T_1[t_2^2(^3T_1)e]$	34591	34600	E''	34706		
	34608		E'	34748		
			E'	37838		
$b^4T_1[t_2e^2(^3A_2)]$	34787	34200	E'	35986		
	34805		E''	35995		
	34970		E''	36949		
	35031		E''	36978		
			E'	37009		
			E'	37061		
$c^2T_2\ [t_2^2(^1T_2)e]$	38933	39000	E''	38260		
	39015		E'	38377		
			E''	41128		
$^2A_2[t_2^2(^1E)e]$	40512		E''	40611	40359	40397
$d^2T_1[t_2e^2(^3A_2)]$	46279					
	46386		E'	48009		
			E''	49637		
			E'	49654		
$e^2T_2[t_2e^2(^1E)]$	47083					
	47217		E'	48387		
			E''	48436		
			E''	50443		

TABLE VII. (*Continued*)

	Cubic			Vacancy		Pair
	Diagonalized	Observed		Diagonalized	Observed	Observed
$c\,^2E[t_2^2(^1A_1)e]$	48 519		E''	47 726		
			E'	50 439		
$e\,^2T_1[t_2e^2(^1E)]$	51 687		E'	52 473		
	51 808		E''	53 525		
			E'	53 527		
$d\,^2T_2[t_2e^2(^1A_1)]$	65 588		E''	64 127		
	65 780		E'	68 436		
			E''	68 611		
$d\,^2E[e^3]$	67 812		E'	70 207		
			E''	72 521		
	$Dq=1590$			$Dq=1645$		
	$B=660$			$B=570$		
	$C=2920$			$C=3165$		
	$\zeta=\zeta'=240$			$\zeta=\zeta'=240$		
	$\alpha=70$			$\alpha=70$		
	$\delta=0$			$\delta=1350$		
	$\mu=0$			$\mu=-3200$		

In the diagonalization, the complete weak-field matrices of Jesson for the d^3 system are used,[18] which include all the terms in Eq. (6). In this basis, H_E rather than H_C is nearly diagonal, as is convenient for free-ion calculations. In this case the weak-field matrices are preferred over the strong-field matrices calculated for the perturbation loops because of the fewer number of matrix elements and because of the ease in incorporating the Trees parameter α which gives a better fit of diagonalization to experiment for Cr^{3+} in other crystals.[7] The crystal field parameter Dq and the electrostatic parameters B and C are varied to give a best fit to experimentally observed levels, and the value of α used is similar to that for Cr^{3+} in other crystals.[7] Note that the best-fit values of Dq, B, and C are different for the cubic and the vacancy systems. The increase in Dq in the vacancy system is consistent with a compressive stress, which should increase the crystal field. A change in the electrostatic interaction is also expected for the changed environment. The value of ζ used (240 cm^{-1}) is slightly larger than that commonly used for Cr^{3+} in other crystals (180–225 cm^{-1}), but it is still less than the free-ion value (273 cm^{-1}). This larger value gives a better fit to the only observed splittings which are sensitive to changes in the value of ζ: the $^4A_2$ state in the vacancy system and the $a\,^2T_1$ state in the cubic system. The diagonalized energies are listed in Table VII and the splittings in Table VI. Since the perturbation loops use the strong-field basis, where a Trees correction is inconvenient, the diagonalization splittings shown in Table VI for comparison are calculated with $\alpha=0$ (which necessitated changing B and C also).

The agreement in Table VI between diagonalization and perturbation theory is very good, demonstrating that the latter approach is useful for the tetragonal field of the vacancy site. The calculated splittings also fit very well the observed splittings of the $^4A_2$, $a\,^2E$, $a\,^2T_2$, $^4T_2$, and $a\,^4T_1$ levels in the MgO:Cr^{3+} vacancy system. This demonstrates the validity of using the estimated band splittings to help determine the parameters.

For the $a\,^2T_1$ levels, the calculations of approximately 250-cm^{-1} splitting for the vacancy system provide further evidence that the observed pair in ground-state absorption split by 58 cm^{-1} is in the cubic rather than the tetragonal vacancy system. This is in better agreement with the cubic diagonalization splitting of 53 cm^{-1} in Table VII. The similarity of the tetragonal-field-splitting calculations for the $a\,^2T_1$ level to the splitting of the lines in the red in the selective-excitation trace for the vacancy and pair system indicates that they could be the $a\,^2T_1$ levels. However, this must still be regarded as uncertain.

Finally, one notes the close agreement of the observed splittings of the vacancy and pair systems. Both systems must therefore have nearly identical tetragonal perturbing fields and similar values of δ and μ. Since the vacancy system has Cr^{3+} ions with vacancies in the [001] direction, the pair system must be composed of Cr^{3+}-vacancy-Cr^{3+} complexes in the [001] direction in order to get a similar tetragonal field.

One is tempted to use the slightly different splittings of the ^2E levels in the pair-vacancy and vacancy systems to estimate the small difference in δ and μ values in the two systems. From these values the shift of the $^2A_2$ level could be compared

to the experimental data to help identify the system involved. However, the $^2A_2$ state is very sensitive to Dq, B, and C parameters which might also change slightly between the vacancy and pair-vacancy environment. Therefore, we can only say that the small shift in energy between the two observed $^2A_2$ levels is consistent with the small shift of other levels between the vacancy and pair systems. The assignment of the $^2A_2$ levels by intensity calculations and varying concentration[7] to the vacancy and pair systems is in accord with this analysis.

V. CONCLUSION

Energy levels in the three MgO:Cr^{3+} systems, cubic site, tetragonal vacancy, and pair-vacancy sites, have thus been analyzed both by perturbation loops and by computer diagonalizations and measured by ground-state absorption and selective-excitation traces. New $^2T_2$ and $^2T_1$ levels seen in ground-state absorption have been assigned to the vacancy (and pair-vacancy) and cubic systems, respectively. Lines tentatively attributed to the $^2T_1$ levels in the vacancy and pair-vacancy systems have also been observed. Better tetragonal-field parameters for the vacancy and pair-vacancy system have been derived. Perturbation loops and diagonalizations agree well with experiment.

ACKNOWLEDGMENTS

The authors are grateful to A. L. Schawlow for advice and encouragement of the project, and to R. M. Macfarlane for many helpful discussions.

---

†Research supported by the National Science Foundation under Grant No. GP-28415 and the Advanced Research Projects Agency through the Center for Materials Research at Stanford.

*N. S. F. Predoctoral Fellow.

‡U. S. Air Force Postdoctoral Fellow. Present address: Molectron Corp., 930 Thompson Pl., Sunnyvale, Calif. 94086.

[1]J. E. Wertz and P. Auzins, Phys. Rev. 106, 484 (1957).

[2]A. L. Schawlow, A. H. Piksis, and S. Sugano, Phys. Rev. 122, 1469 (1961).

[3]G. F. Imbusch, W. M. Yen, and A. L. Schawlow, Phys. Rev. 133, A1029 (1964).

[4]G. F. Imbusch, Ph.D. dissertation (Stanford University, 1964) (unpublished).

[5]G. F. Imbusch, A. L. Schawlow, A. D. May, and S. Sugano, Phys. Rev. 140, A830 (1965).

[6]R. M. Macfarlane, J. Chem. Phys. 47, 2066 (1967).

[7]G. K. Klauminzer, W. M. Fairbank, Jr., and A. L. Schawlow (unpublished).

[8]Sample No. 1: $\frac{1}{2}$-in.-diam×3-cm-long cylinder, 0.061-wt% Cr_2O_3 from Norton; sample No. 2: $\frac{1}{2}$-in.-diam×$\frac{3}{8}$-in.-long cylinder, 0.018-wt% Cr_2O_3 from Materials Research Corp.; sample No. 3: $\frac{5}{16}$-in.-diam×$\frac{3}{8}$-in.-long cylinder, 0.22-wt% Cr_2O_3 from Norton; sample No. 4: 0.236×0.378×0.540-in. rectangular solid, 0.22-wt% Cr_2O_3 from Norton.

[9]M. D. Sturge, H. J. Guggenheim, and M. H. L. Pryce, Phys. Rev. B 2, 2459 (1970).

[10]δ and μ are the tetragonal-field splittings of a single d electron in the cubic t_2 and e states, respectively, as defined in J. S. Griffith, *The Theory of Transition Metal Ions* (Cambridge U. P., Cambridge, England, 1961), p. 342, hereafter designated as GI.

[11]L. I. Schiff, *Quantum Mechanics*, 3rd ed. (McGraw-hill, New York, 1968).

[12]J. S. Griffith, *The Irreducible Tensor Method for Molecular Symmetry Groups* (Prentice-Hall, Englewood Cliffs, N. J., 1962), hereafter designated as GII.

[13]Y. Tanabe and S. Sugano, J. Phys. Soc. Japan 9, 753 (1954).

[14]Y. Tanabe and H. Kamimura, J. Phys. Soc. Japan 13, 394 (1958).

[15]S. Sugano, Y. Tanabe, and H. Kamimura, *Multiplets of Transition-Metal Ions in Crystals* (Academic, New York, 1970).

[16]M. D. Sturge, Solid State Phys. 20, 91 (1967).

[17]A. L. Schawlow, J. Appl. Phys. 33, (1962).

[18]J. P. Jesson, J. Chem. Phys. 48, 16 (1968).